



One-Pot Synthesis of Iron-Containing Nanoreactors with Controllable Catalytic Activity Based on Multichannel Mesoporous Silica

Haiqing Wang, Xiaoming Li, Cuirong Xiong, Shuying Gao, Jun Wang,* and Yan Kong*[a]

We have constructed Fe-substituted silicate nanotube reactors (Fe-NTRs) through a newly developed one-step solubilization (OSS) method in which cetyltrimethylammonium bromide and P123 are used as structure-directing and shape-controlling agents, respectively, and ferrocene is utilized as iron source by solubilizing inside the hydrophobic inner core of the surfactant micelles. The Fe-NTRs showed regular morphology, highly ordered multichannel mesopores, controllable sizes with lengths changing from 150 nm to 1.2 μm , diameters of approximately

130 nm and pore sizes of approximately 2.7 nm, and iron contents in a range from 0.66 to 1.59 wt%. The OSS strategy is also applicable for other metal-functioned silicate nanoreactors. The catalytic activity of Fe-NTRs in the direct hydroxylation of phenol can be essentially manipulated by the controllable sizes. The release behavior of reactants reveals that the diffusion control derived from the lengths of Fe-NTR should be responsible for the resultant reactivity.

Introduction

Nanoreactors have received a lot of attention in recent years owing to their multifunctionality in various catalysis applications.^[1,2] In principle, the construction of nanoreactors require elaborate active sites and a controllable nanostructure. Their catalytic performance (e.g., conversion, yield, selectivity, and product distribution) can be manipulated in a controllable manner by tuning the local nanostructures, such as morphology, size, or composition^[3,4-9] due to the confined space, particle size, and morphology-dependent reaction kinetics.^[10] To achieve these essential catalytic structures with a high degree of control, the nanosynthesis techniques of catalysts are crucial, however, they remain technically challenging.

Mesoporous silica nanoparticles (MSNs) have been extensively studied owing to their excellent texture characteristics such as large pore volume, high surface area, well-ordered pore size (2–50 nm), flexible mesostructure, diverse surface functionality, and good biocompatibility.^[5,11] These properties of MSNs make them attractive as hosts for nanocatalysis. At present, pure MSNs with various morphologies including sphere, helix, fiber, rod/tube, hollow, crystal, and other special morphologies have been obtained.^[12,13] To further enhance the inherent properties and endow MSNs with multifunctionality, it is important to achieve morphology and size control while

maintaining the ordered mesostructures.^[1,14] Recent studies indicated that the tubular particles with multiple nanochannels can be used as an ideal nanoreactor for nanocatalysis, because each array of nanochannels can be regarded as a reactor and the nanochannel can exert more enhanced confinement effect.^[9,15,16] However, the effective control of multichannel silica nanotubes by means of direct synthesis was poorly defined.^[17]

Previous works have revealed that the Fe, Ti, and Zr-containing silicate catalysts are of academic and industrial interest for their versatility in many important reactions, such as alkylation, cracking, isomerization, aromatics oxidation, Fenton reaction, Friedel–Crafts acylation, and Fischer–Tropsch synthesis.^[7,8,16,18] However, the shape-controlled synthesis of the abovementioned catalysts combined with ordered mesopores is rarely achieved. The syntheses of Fe, Ti, and Zr-containing nanoreactors are totally different from that of the recently obtained copper-containing nanotube reactor,^[19] which can be constructed by controlling the simultaneous hydrolysis of copper and silicon sources by the formation of copper–ammonia complex aqueous solution. Apparently, the synthetic approach cannot be widely adapted for other inorganic transition metal sources because the precipitates are usually formed under alkaline conditions. Moreover, the inorganic metal salts have revealed more adverse effects on the original shape of surfactant micelles and caused the assembly of silica monomers by exotic electrostatic interactions, which inevitably destructed the morphology and mesopores of the resultant metal-containing silicate materials.^[20,21] Taken together, the fabrication of mesoporous silicate nanoreactors requires (i) an effective and flexible strategy for the controllable synthesis of materials; (ii) a suitable silicon and metal source; (iii) precisely controlled synthesis parameters. The one-step synthesis of a real mesoporous sili-

[a] Dr. H. Wang, X. Li, C. Xiong, S. Gao, Dr. Prof. J. Wang, Dr. Prof. Y. Kong
State Key Laboratory of Materials-Oriented Chemical Engineering
College of Chemistry and Chemical Engineering
Nanjing Tech University
Nanjing 210009 (P.R. China)
Fax: (+86) 25-83587860
E-mail: kongy36@njtech.edu.cn
junwang@njut.edu.cn

Supporting information for this article is available on the WWW under <http://dx.doi.org/10.1002/cctc.201500868>.

cate nanoreactor with transition-metal functionality and regular multichannel tubular morphology has been rarely reported owing to the limitations in the design of the support and active site.

Herein, we report on the development of a new one-step solubilization (OSS) process to construct iron-doped multichannel mesoporous silica nanotube reactors (Fe-NTRs) with controllable nanostructures. The broader applicability of OSS strategy was demonstrated by using other metallocenes as metal sources. The effects of iron contents and sizes of Fe-NTRs on the catalytic activity were investigated in the direct hydroxylation of phenol with H_2O_2 as oxidant.

Results and Discussion

OSS strategy: in situ incorporation of iron into mesoporous silica

Our proposed new OSS strategy can be described as the process given in Figure 1. The original mixture consisted of cetyl-

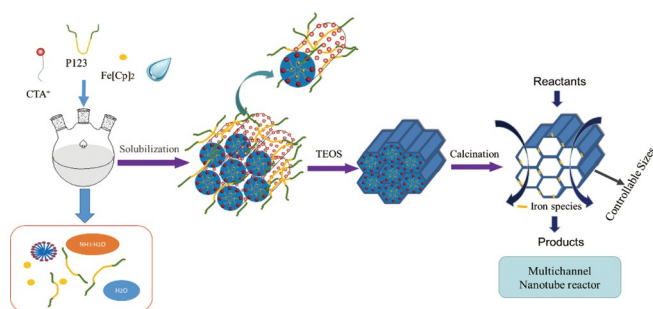


Figure 1. Illustration of OSS strategy.

trimethylammonium bromide (CTAB), $\text{PEO}_{20}\text{PPO}_{70}\text{PEO}_{20}$ (P123, $M_n \approx 5800$), and ferrocene in ammonia. The ferrocene molecules were preferentially solubilized inside the hydrophobic core of SDA micelles, because of their insolubility in water. A small amount of P123 was used as an additive for the control over the size and morphology of Fe-NTRs. The micelles solubilizing ferrocene were stacked into hexagonal array (Step I). After the addition of silica source, the hydrolyzed silicate species were assembled into inorganic silica framework around these micellar arrays, as shown in Step II. Then, the precursor of organ-iron compound was confined in the nanochannels of silicate. During the removal of the surfactants by calcination at 550°C for 6 h (Step III), ferrocene molecules were decomposed into inorganic iron species. Finally, the iron-incorporated silicate materials with regular morphology and ordered mesopores were achieved.

To verify the OSS strategy, that is, the solubilization of ferrocene inside the hydrophobic core of surfactant micelles, we conducted control experiments. As shown in Table 1, the iron contents exhibited an upward trend from 0.50 to 0.81 wt% with increasing amount of CTAB from 0.2 to 0.8 g. This finding should be ascribed to the improved solubilization of ferrocene

Table 1. The iron content in samples with different addition amount of CTAB or TEOS.

Sample ^[a]	Iron content [wt %]	Sample	Iron content [wt %]
0.2, 0.02, 2.0	0.50	0.4, 0.06, 1.0	0.70
0.4, 0.02, 2.0	0.65	0.4, 0.06, 2.0	0.65
0.8, 0.02, 2.0	0.81	0.4, 0.06, 3.0	0.58

[a] CTAB (g), P123 (g), TEOS (mL)

inside the hydrophobic core of CTAB micelles. In contrast, the increased amount of tetraethylorthosilicate (TEOS) led to the decrease of iron content from 0.70 to 0.58 wt%. The latter should result from the presence of ethanol in the solution after the addition of TEOS. Ethanol increases the solubility of ferrocene and leaches the organo-metal complex outside the micelles, resulting in the lower iron content. This result indicates that in the OSS procedure the iron species were incorporated into the mesopores of materials by the solubilization of ferrocene molecules inside the hydrophobic core of CTAB micelles. The FTIR spectra (see Figure 3) and structural parameter results (see Table 2) further support the OSS strategy, which will be discussed below.

Mesostructure

The small-angle XRD patterns of the parent mesoporous silica and Fe-NTR samples (5R1, 5R2, 5R3, 5R4, and 5R5 with varied length; 10, 15, and 20R3 with altered iron contents, see Experimental Section for details) are shown in Figure 2a and 2b, respectively. The sharp (100) reflection peak at $2\theta = 2.0$ to 2.5° demonstrates the characteristics of a typical mesoporous structure. Three other weak peaks, indexed to the (110), (200), and (210) reflections,^[22] confirmed the presence of a highly ordered $P6mm$ 2D hexagonal mesophase.^[23] Compared with pure samples, the typical hexagonal structure of Fe-NTRs was clearly observed, which indicates that by using this new OSS strategy, the highly ordered mesopore structure was well retained in the iron-containing Fe-NTR samples. All the diffraction peaks of Fe-NTRs shift to lower angles, indicating the enlarged structure units.^[4,8] This observation is an evidence of the ferrocene molecules solubilizing into the hydrophobic region of CTA^+ micelles. Sample 5R5 show relatively low reflections suggesting the reduced ordering degree of its mesostructure.^[7] For the Fe-NTRs with altered iron content (Figure 2b), the peaks of 20R3 shifted to higher angles, which may be caused by the formation of extra-framework iron species.^[7,20] The amount of ferrocene that can be solubilized by CTAB micelles is limited. For sample 25R3 with over 2.5 wt% iron content, only one broad (100) peak (Supporting Information, Figure S1) could be observed, and the (110) and (200) reflections disappeared. No reflections for 40R-3 (Figure S1) were detected suggesting a complete loss of mesopores. These observations indicate that higher input amount of ferrocene can lead to a reduced order degree of mesostructure of Fe-NTRs.

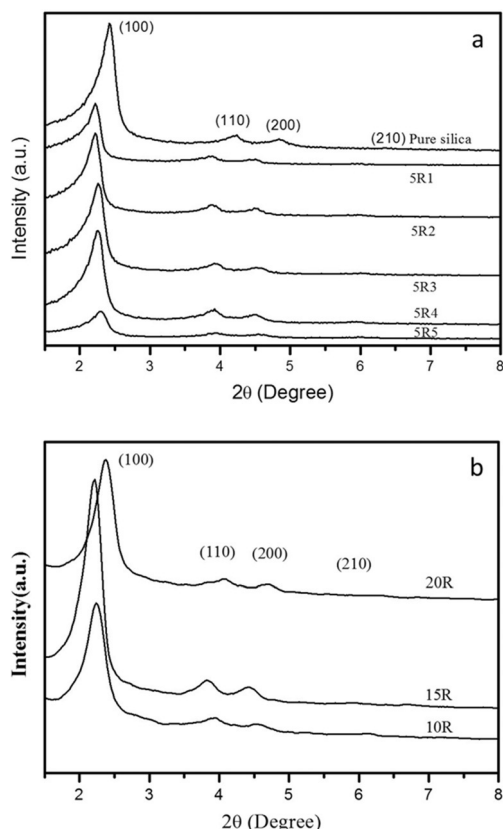


Figure 2. XRD patterns of a) pure silica, samples 5R1, 5R2, 5R3, 5R4, and 5R5; b) 10, 15, and 20R.

In contrast, the mesoporous structure of Fe-NTRs were highly ordered if a moderate amount of ferrocene was used.

FTIR spectra of ferrocene, as-synthesized pure sample (without ferrocene), as-synthesized 5R2 and calcined 5R2 are shown in Figure 3. Compared with the spectra of ferrocene and as-synthesized pure sample, the remarkable peak at 1380 cm^{-1} should be assigned to the stretching vibration of C=C in ferrocene,^[24] indicating the incorporation of ferrocene molecules into the materials during the synthesis procedure. This further supports our proposed OSS synthetic process of

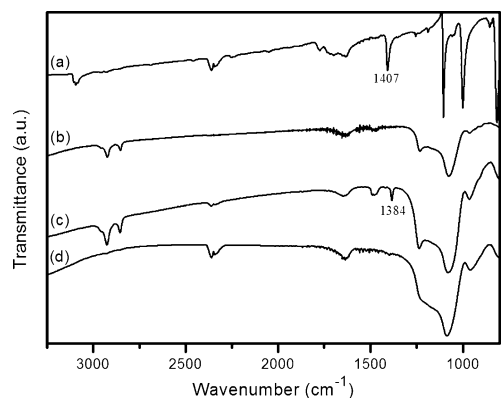


Figure 3. FTIR spectra of a) ferrocene, b) as-synthesized silica (without ferrocene), c) as-synthesized 5R2, and d) calcined 5R2.

Fe-NTRs. The characteristic bands of C–H at 2921 cm^{-1} and 2852 cm^{-1} disappeared in calcined 5R2, suggesting the total removal of template after calcination at 550°C for 6 h.^[7] The complete decomposition of ferrocene to inorganic iron species was confirmed by the disappearance of C=C vibration band at 1384 cm^{-1} .

N₂ physisorption

The structure parameters of the obtained materials were evaluated by nitrogen physisorption isotherms. As shown in Figure 4, all Fe-NTRs exhibited nitrogen adsorption-desorption

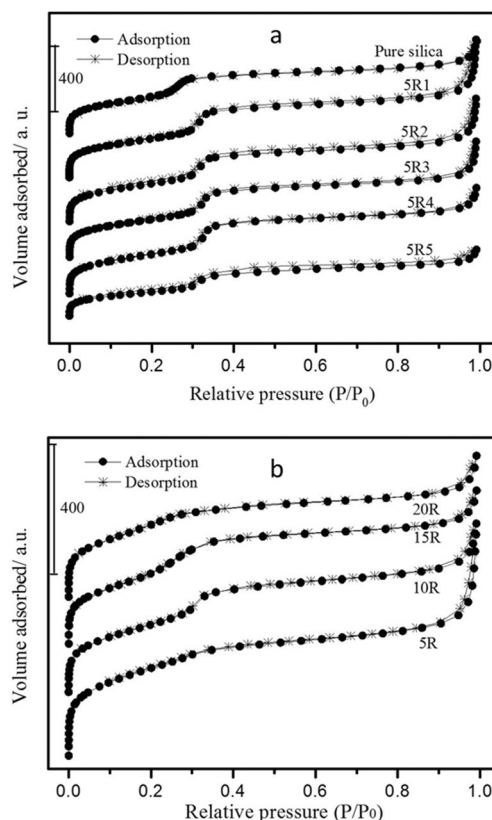


Figure 4. Nitrogen adsorption-desorption isotherms of Fe-NTRs.

isothermal curves similar to that of the pure mesoporous silica. Their type IV isotherms together with a sharp inflection at relative P/P_0 between 0.2 and 0.4, indicate the presence of uniform cylindrical mesopores and very narrow pore-size distributions.^[25] The second capillary condensation step above 0.95 in the adsorption branch was observed more apparently from 5R5 to 5R1 (Figure 4a), which is attributed to the interparticle voids, indicating the smaller particle size.^[26] Sample 5R5 showed relatively low amount of physisorbed nitrogen indicating a reduced ordering degree of mesopores, in agreement with the XRD pattern of 5R5. These observations indicated that the ordered multichannel structure was well preserved in the iron-containing samples, which accorded well with the results of XRD. Compared with pure sample synthesized without

ferrocene, the capillary condensation step in Fe–NTRs shifted toward a relatively higher relative pressure, which indicates a bigger pore size.^[7] Sample 5R3 showed an increase of approximately 0.3 nm in the pore size, as listed in Table 2, which

Sample	D_{100} [nm]	a_0 [nm]	D_p [nm]	W_t [nm]	S_{BET} [m ² g ⁻¹]	Total pore volume [cm ³ g ⁻¹]
pure silica	3.65	4.22	2.37	1.85	985	0.89
5R1	3.98	4.60	2.71	1.89	965	1.34
5R2	3.98	4.60	2.71	1.89	949	1.15
5R3	3.91	4.51	2.70	1.81	917	1.12
5R4	3.91	4.51	2.71	1.81	901	1.03
5R5	3.88	4.47	2.70	1.77	619	0.66

should be due to the introduction of ferrocene inside the hydrophobic core of CTAB micelles. These findings demonstrated the correctness of the new OSS strategy. Some structural parameters of samples 10R, 15R, and 20R are listed in Table 3.

Sample	D_{100} [nm]	a_0 [nm]	D_p [nm]	W_t [nm]	S_{BET} [m ² g ⁻¹]	Total pore volume [cm ³ g ⁻¹]
10R	3.91	4.51	2.62	1.89	908	0.83
15R	3.98	4.59	2.57	2.02	859	0.76
20R	3.65	4.22	2.12	2.10	842	0.70

For samples 15R3 and 20R3, the pore sizes, the specific area, and the total pore volume were reduced with the increase of iron content, which should be ascribed to the formation of iron oxide on the channel surface of materials.^[4,7]

The results of aforementioned characterizations show that by using the OSS method, the iron species were successfully incorporated into the mesopores of Fe–NTRs. The ordered multichannel mesopore structure of the original samples can be well-preserved in the iron-containing samples (Fe–NTRs).

Morphology

The SEM images of samples 5R (i.e., 5R2), 10R, 15R, and 20R with variations in iron contents are revealed in Figure 5. Note that if an inorganic iron source such as FeCl₃ was used, a bronzing precipitation of ferric hydroxide (Fe(OH)₃) was quickly generated. The resultant silicate sample showed monolithic irregular morphology, not shown here. In contrast, it is apparent that the resultant particles in Figure 5 are well-monodispersed and exhibit regularly tubular morphology. The tubes have an average size of 300 nm in length and 130 nm in diameter. Compared with the pure sample (Figure S2a) synthesized with the same amount of CTAB and P123, these samples showed similar size, indicating that the addition of ferrocene exhibited negligible effects on the morphology of Fe–NTRs. Note that although the hexagonal mesophase of sample 40R was collapsed (as re-

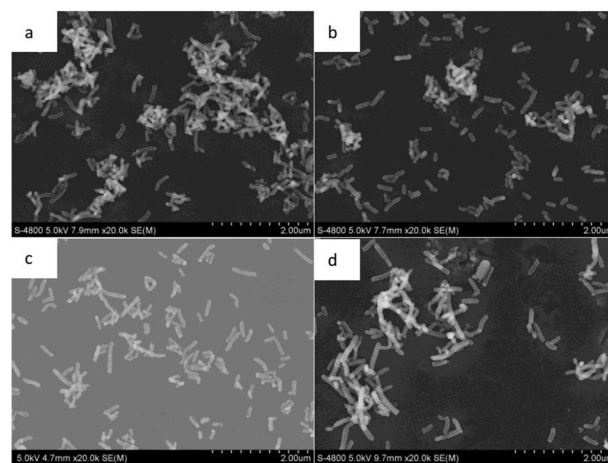


Figure 5. SEM images of Fe–NTRs: a) 5R (i.e., 5R2), b) 10R, c) 15R, and d) 20R.

flected in Figure S1), the tubular morphology was still maintained (in Figure S2b), indicating that the overloading of iron precursor only destructs the local ordering of CTAB micelles. These observations demonstrated that the morphology of Fe–NTRs can be well-preserved with the OSS strategy.

Samples 5R1, 5R2, 5R3, 5R4, and 5R5 were obtained by altering the concentration of shape-controlling additive. The effect of the concentration of P123 on the particle morphology and size was investigated with SEM. As shown in Figure 6, the tube morphology of 5R_n samples are found to be uniform throughout the products. With a decrease in [P123] from 2.59×10^{-1} mM to 3.45×10^{-2} mM, it is clear that the lengths of samples 5R1 to 5R5 were increased from 150 nm to 300 nm, 600 nm, 800 nm, and 1.2 μ m. Considering the lower order degree of mesopores in 5R5, as reflected in XRD pattern and nitrogen physisorption isotherm, it was suggested that local destruction effect of ferrocene should be more evident with the increased length of samples. Samples have a similar outer diameter of approximately 130 nm. The aforementioned results indicated that the shape-controlling additive P123 endowed the Fe–NTRs with controllable sizes. The sizes and the changing trend of Fe–NTRs with varied [P123] were summarized in Figure 6e. The P123 micelles had a hydrodynamic radius of approximately 9.8 nm, whereas all Fe–NTRs displayed a pore size of approximately 2.7 nm, which indicates that the P123 may not enter into the micelles. Moreover, the break-up of P123 micelles usually happens at high ionic surfactant concentrations.^[27] We suggest that the hexagonal mesostructure of Fe–NTRs was predominantly constructed by the strong electrostatic interactions between negatively charged silicates and positively charged CTA⁺ micelles.^[28] The P123 molecules may reside at the outer surface of micelles of CTAB. If the molar ratio of P123/CTAB was further increased, more end-face coverage of P123 molecules will ultimately decrease the length of micelles and realize the controllable formation of Fe–NTRs. Therefore, the P123 molecules should act as a shape-controlling additive to modulate the morphology and size of Fe–NTRs. Elemental mapping by energy-dispersive X-ray spectro-

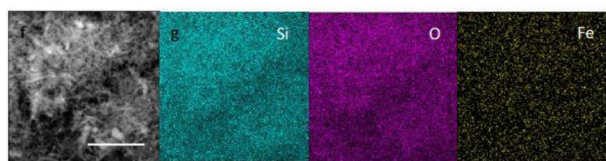
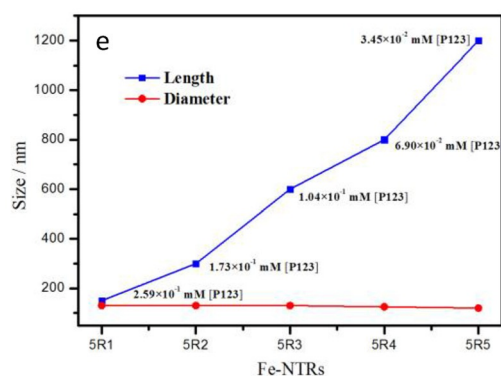
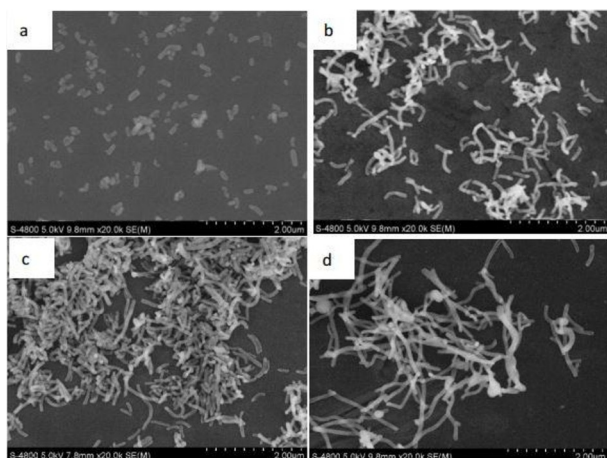


Figure 6. SEM images of Fe-NTRs: a) 5R1, b) 5R3, c) 5R4, d) 5R5, e) the size variation of Fe-NTRs with [P123], f,g) EDX elemental mapping of aggregated 5R3 without ultrasonic treatment (SEM image (g), scale bar is 1 μm).

copy (EDX) shows that the elements Si, O, and Fe are homogeneously distributed throughout the whole particle (Figure 6 g). To the best of our knowledge, this is the first report for the controllable preparation of metal-containing mesoporous silicate nanotube nanoreactor (Fe-NTRs) by a one-step method. Taken together, in this new procedure, the OSS strategy preserved the ordered multichannel structure and original tube morphology of particles. In addition, the shape-controlling additive P123 provided an effective and flexible route for the precise design of nanoreactors.

High-resolution transmission electron microscopy (HRTEM)

TEM images of the representative Fe-NTRs: 5R1, 5R3, 5R5, and 10R are depicted in Figure 7. The hexagonal honeycomb-like mesostructure of Fe-NTR was well-defined as seen in the top view of 5R3 (Figure 7b, upper inset). The selected-area electron diffraction pattern (SAED, Figure 7b, lower inset) dem-

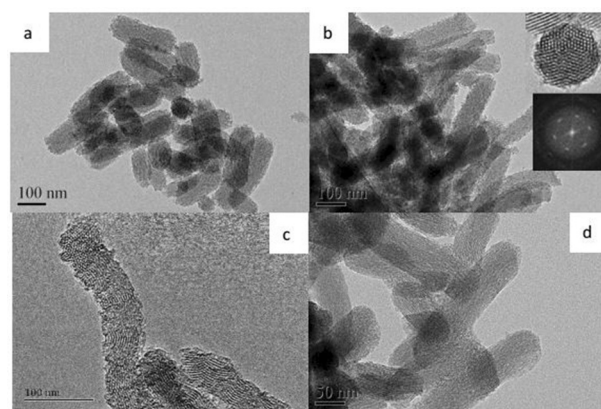


Figure 7. TEM images of the representative Fe-NTRs: a) 5R1, b) 5R3, c) 5R5, and d) 10R. The insets in (b) give the top view (top) and the SAED pattern (bottom).

onstrates the highly ordered 2D-hexagonal channel arrangement of materials. The well-ordered multichannel structure of 5R1, 5R3, and 10R was clearly visualized in a side view (Figure 7a, b, and d), and the mesostructure of 5R5 appears slightly disordered (Figure 7c), according well with the results of XRD and N_2 physisorption. The pore sizes were found to be in the range of 2.6–2.8 nm, in good agreement with the D_p results calculated from the BJH model using desorption data (Table 2). Each hexagonal unit of the paralleled pore structures can be regarded as a nanochannel reactor. In contrast, the mesopores of 25R3 with higher iron content (TEM, Figure S3) are less ordered in hexagonal arrays, which accords with the XRD result. These observations indicate that the Fe-NTRs with OSS process can maintain the tubelike morphology as well as the ordered hexagonal mesostructure of the parent silica. Note that iron oxide particles are clearly observed with the direct calcination of ferrocene. However, no iron oxide particles or aggregations are detected outside or inside the channels of Fe-NTR. The iron species are highly dispersed into the channels, which should ascribe to the confinement of silicate nanochannel, indicating the introduced iron active centers are highly accessible to guest molecules.

To demonstrate the applicability of the OSS strategy, titanocene dichloride and zirconocene dichloride were used for preparing Ti and Zr-containing mesoporous silicate, whereby a molar ratio of metallocene/silicon = 0.05 was used in the synthesis gel. The four well-defined reflection peaks in XRD pattern (Figure S4a and b) indicate the presence of highly ordered mesoporous channels in the Ti and Zr-containing reactors. The Ti and Zr contents are 0.051 wt% and 0.047 wt%, respectively. UV/Vis diffuse reflectance (Figure S4c and d) spectroscopy suggests the formation of the framework $\text{Ti}^{[29]}$ and $\text{Zr}^{[30]}$ species in the mesoporous silicate reactors. As shown in Figure S5, the TEM images of Ti- and Zr-NTR illustrate a highly ordered multichannel mesoporous structure and regular tube morphology. The result indicates that this new OSS strategy is broadly applicable to the preparation of various metal-containing silicate nanoreactors for practical applications. Potentially, this method can endow nanoreactor with two different metals within one

assembly, which will attract special attention because of potential synergic effects of different metals for a variety of advanced applications.^[31]

The states of iron species

UV/Vis spectroscopy is a very effective method for the characterization of coordinated environment of iron species in silicate materials. The UV/Vis diffuse reflectance spectra in the wavelength range of 230–650 nm of some samples are shown in Figure 8. Note that no absorption band is present for the

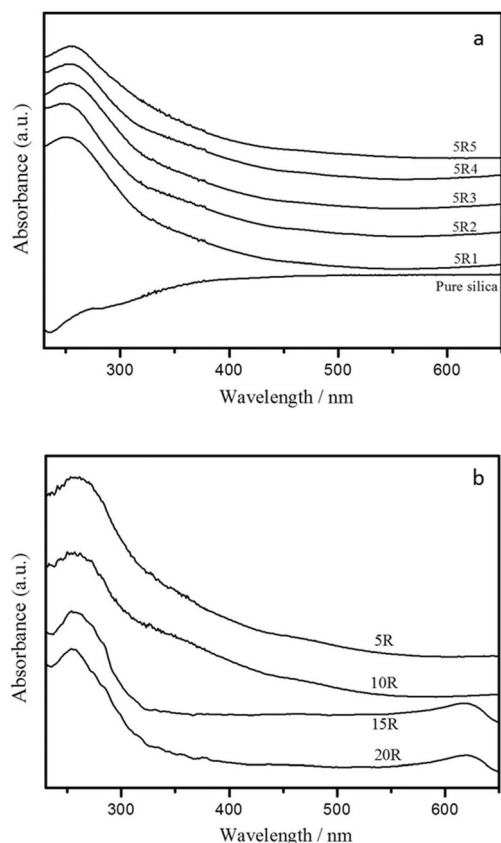


Figure 8. UV/Vis absorption spectra for the Fe-NTRs: a) pure silica, 5R1, 5R2, 5R3, 5R4, and 5R5; b) 10R, 15R, and 20R.

parent mesoporous silica. A broad band between 230 nm and 300 nm centered at 255 nm, assigned to the low-energy $d_{\Pi}-p_{\Pi}$ charge-transfer transitions between tetrahedral oxygen ligands and central Fe^{3+} ion, was observed for all samples.^[7,32] This band demonstrated that the bonds of Fe–O–Si were formed and most of iron atoms existed in the framework of silicate.^[20] A shoulder band at around 330 nm indicates the presence of polyferrate $(Fe-O-Fe)_n$ on the silicate surface.^[33] The broad band between 400 and 550 nm should be ascribed to highly dispersed extra-framework iron oligomer.^[7] The observations from the UV/Vis spectra indicate that for Fe-NTRs with iron content of 0.6 wt%, most iron atoms are incorporated into the framework of Fe-NTRs in the form of isolated iron species and only very few extra-framework iron species were highly dis-

persed on the channel surface of the samples. In Figure 8b, for the samples 15R and 20R, if the content of iron reached more than 1.18 wt% (in Table 4), the extra broad absorption band

Table 4. Catalytic activity of Fe-NTRs: 5R, 10R, 15R, and 20R in the phenol hydroxylation to dihydroxybenzene.

Sample	Iron content ^[a] [wt %]	χ ^[b] [%]	S ^[c] [%]	γ ^[d] [%]	Cat./Hyd. ^[e]
5R	0.66	42.4	57.3	24.3	1.52
10R	0.98	51.3	47.6	24.4	1.61
15R	1.18	29.4	30.1	8.8	1.43
20R	1.59	15.2	23.5	3.6	1.64
Fe_2O_3	–	9.8	18.6	1.8	1.70

[a] ICP results. [b] Phenol conversion. [c] Dihydroxybenzene selectivity. [d] Yield. [e] Molar ratio of catechol/hydroquinone.

between 600 and 650 were detected indicating that the existence of aggregated Fe_2O_3 particles.^[6] However, no characteristic peaks of iron oxides were found in high-angle XRD patterns (not shown here), suggesting that the introduced iron species by OSS procedure should be incorporated into the framework of silica or highly dispersed on the wall of nanoreactor.^[4,7] This result should be ascribed to the fact that the interactions between ferrocene molecules were weakened when being solubilized inside the hydrophobic core of CTAB micelles. As a result, the dispersion degree of iron species was improved.

X-ray photoelectron spectroscopy (XPS)

The calcined Fe-NTRs were characterized by XPS technique. In Figure 9 the Fe 2p XPS spectra of the representative 5R and

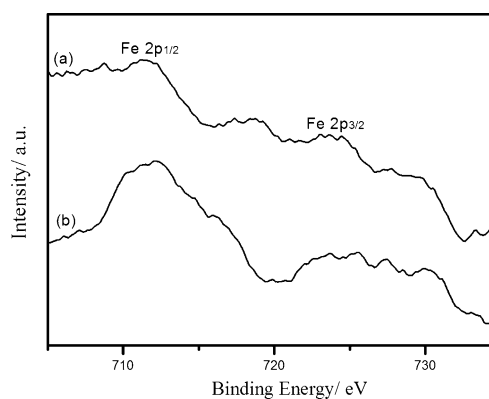


Figure 9. XPS spectra of Fe 2p Fe-NTRs: a) 5R and b) 20R.

20R samples are given. Two peaks assigned to $Fe2p_{3/2}$ (≈ 712 eV) and $Fe2p_{1/2}$ (≈ 725.0 eV) are clearly observed for the iron-containing samples, which indicate the presence of Fe^{3+} .^[33–35] The other peaks are attributed to shake-up satellites of the $2p_{3/2}$ and $2p_{1/2}$ peaks.^[35] The binding energy of the pure iron oxide is approximately 710.8 eV and 724.2 eV, respectively.^[7] In contrast, the $Fe2p_{3/2}$ and $Fe2p_{1/2}$ of all Fe-containing

samples show a little positive shift of 0.8–1.0 eV in binding energy, which may be attributed to the higher electronegativity of silicon than iron.^[7] The result indicates the incorporation of iron atoms into the silicate framework,^[35] which accords well with the UV/Vis spectroscopy observations. The two peaks of 20R became broader and more intensive, indicating an increasing iron content in the samples.^[7,35] Moreover, the bulk iron content and the surface iron content in sample 20R (1.59 wt%) are 0.017 and 0.009 determined by inductively coupled plasma mass spectrometry (ICP-MS) and XPS, respectively. As for the 5R (0.65 wt%) with lower iron loading amount, the bulk iron content (molar ratio of Fe/Si=0.007) is higher than 0.002 of surface iron content obtained from XPS. This observation indicates, with the increasing amount of iron loading, more extra-framework iron species were produced. In the case of lower iron loading amount, most of iron species are incorporated into the silicate framework of Fe-NTRs. These findings further support the conclusion obtained from UV/Vis spectroscopy.

Catalytic performance

The catalytic activity of the produced Fe-NTRs was examined by the one-step hydroxylation of phenol to dihydroxybenzene with H₂O₂ as an oxidant.

Effects of iron content

The effects of iron content were evaluated based on the Fe-NTRs 5R, 10R, 15R, and 20R. The results were summarized in Table 4. Pure mesoporous silica nanotube showed no catalytic activity because of the absence of active sites. If using the iron-containing samples, the catalytic activity was remarkably improved, which indicates that the iron species should be responsible for the phenol hydroxylation reaction. From the catalytic activity of Fe-NTRs with the same morphology, we found that with the increasing loading amount of iron, the conversion rate of phenol increases first from 48.8% of 5R to 51.3% of 10R, and then decreases to approximately 29.4% of 15R and 15.2% of 20R. The selectivity to dihydroxybenzene decreased gradually from 55.6% of 5R to 47.6% of 10R, 30.1% of 15R, and 23.5% of 20R. Free Fe₂O₃ nanoparticles, often used as reference catalysts for similar reactions, show relatively low activities. For the 5R and 10R samples, their catalytic activities are highly related to the amount of iron. As revealed by UV/Vis spectroscopy, most of iron species in Fe-NTRs 5R and 10R were incorporated in the silicate framework existing in the form of tetra-coordinated iron. This observation indicates that the framework iron species should act as active sites in phenol hydroxylation. However, despite the improved iron content, 15R and 20R showed a dramatic decrease in phenol conversion and dihydroxybenzene selectivity. The oligomeric iron of extra-framework was detected in UV/Vis spectra for samples 15R and 20R. The reduced conversion rate of phenol should be ascribed to the fact that the accessibility to the framework iron was limited by the extra-framework oligomer of iron species. Moreover, the extra-framework iron species contributed

to side-reaction such as the deep oxidation of phenol.^[7] As a result, the selectivity to dihydroxybenzene was dropped with the increasing amount of extra-framework iron species. Although the existence of extra-framework iron is evident, the catalytic activity showed in 15R and 20R can demonstrate that extra-framework iron species were highly dispersed in agreement with the result of high-angle XRD. The aforementioned results indicate that the iron species with tetrahedral coordination in the framework of Fe-NTR were effective for the phenol hydroxylation reaction. In contrast, the oligomeric extra-framework iron results in the lower conversion rate of phenol and dihydroxybenzene selectivity.

Effects of morphology

The effects of the morphology of Fe-NTRs on the catalytic activity in phenol hydroxylation were studied by using 5R1, 5R2, 5R3, 5R4, and 5R5 with different length as catalysts. As shown in Table 5, the conversion rate of phenol first went up from

Table 5. Catalytic activity of Fe-NTRs: 5R1, 5R3, 5R4, and 5R5.

Samples	Length [μm]	Iron content [wt%]	X [%]	S [%]	Y [%]	Cat./Hyd.
5R1	0.15	0.68	35.5	61.8	21.9	1.55
5R3	0.60	0.65	48.8	55.6	27.1	1.49
5R4	0.80	0.65	50.1	50.5	25.3	1.48
5R5	1.20	0.65	40.6	47.2	19.2	1.42

35.5% to 50.1%, as the lengths of samples 5R1 to 5R4 increased from 150 nm to 800 nm, and then decreased to 40.6% of 5R5 with 1.2 μm in length. In contrast, the selectivity to dihydroxybenzene of samples from 5R1 to 5R4 decreased gradually from 61.8% to 47.2%. The Fe-NTR 5R3 with 600 nm in length exhibited the highest yield of 27.1% with 48.8% conversion of phenol and 55.6% selectivity to dihydroxybenzene under the reaction condition.

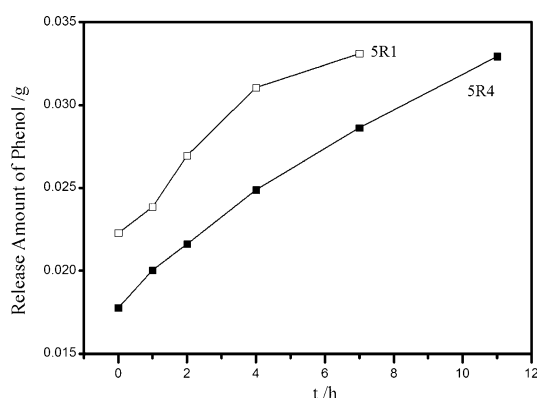
It is generally known that the performance of a catalyst is often related to the amount of active sites, morphology, and structural parameters of the support.^[4,6,7,36] As for 5R5, the decreased degree of order of mesostructure, as reflected by XRD patterns and N₂ physisorption isotherms, should be the reason for its lower catalytic activity. In contrast, for samples 5R1 to 5R4, the total pore volume and BET specific surface area decrease from 1.34 to 1.03 cm³g⁻¹ and from 965 to 901 m²g⁻¹ (Table 2), respectively, with the increasing length of Fe-NTRs. The four samples were similar in the iron content and the valence state of iron species. The catalytic activity should drop according to the present analysis. Therefore, the unexpected dependence of the catalytic activity of materials on the mesostructure suggests that the altered lengths of Fe-NTRs should be responsible for the resultant catalytic activity. It is well-known that mass transfer is an important factor in heterogeneous catalysis, and closely related to the particle sizes. The inner channels of mesoporous silica should be relatively hydrophilic owing to the presence of abundant silanol groups.^[12] The sol-

Table 6. Comparison of the catalytic performance of iron-containing mesoporous silica-based catalysts in phenol hydroxylation to dihydroxybenzene.

Catalysts	Fe/Si ^[a]	Morphology	Reaction conditions	Phenol/H ₂ O ₂ ^[c]	X [%]	S [%]	Y [%]	Ref.
Fe-NTRs (5R3)	0.007	tube	20 ^[b] /25 °C/5 h/20 mg	3:2	48.8	55.6	27.1	
8Fe	0.091	irregular	20 ^[b] /20 °C/3 h/50 mg	3:1	25.3	78.4	20.0	[20]
2Fe-Si	0.02	irregular	10 ^[b] /25 °C/1.5 h/100 mg	1:1	20.1	73.3	14.8	[7]
Fe-MCM-41 NPs(120)	0.008	sphere (120 nm)	20 ^[b] /60 °C/3 h/50 mg	3:1	≈20.0	≈90.0	18.0	[32]

[a] Molar ratio of Fe/Si, [b] Weight ratio of phenol/catalyst. [c] Molar ratio of phenol/H₂O₂.

vent water is expected to be competing with the reactant phenol for the adsorption on the active sites.^[37] We suggested that the increasing length of nanoreactor inevitably enhanced the inner diffusion time of reactants. As a result, the effective absorbance of phenol onto the active centers was promoted, and the conversion rate of phenol was enhanced accordingly. This result is consistent with the finding of Somorjai and coworkers^[38] that the reactivity can be enhanced by increasing the residence time of the reactants in fixed-bed plug flow reactor. Moreover, the release profiles of phenol loaded Fe-NTRs were studied in test tubes. Release profiles of typical 5R1 and 5R4 with different lengths are shown in Figure 10. 5R1 and

**Figure 10.** Release profiles of typical 5R1 and 5R4 with different lengths.

5R4 exhibit the similar maximum release amounts of 0.033 g phenol at 7 h and 11 h, respectively. These findings suggested the diffusion properties of reactants can be well tailored by finely controlling the sizes of nanoreactors and the longer Fe-NTR showed advantages in promoting the presence time of reactants in nanoreactor. This could result in different catalytic behaviors. Longer diffusion time inside the channels of Fe-NTRs was unfavorable to the selectivity to dihydroxybenzene, due to the existence of small amount of iron oxide species. Moreover, the Fe-NTRs showed a potential regulation for catechol/hydroquinone ratio, which decreased with the lengths of Fe-NTRs, because the longer channels should be more favorable for the diffusion of hydroquinone. These findings exhibited that the catalytic activity of catalysts as well as the product distribution can be well-regulated by fine control over size and morphology of materials, suggesting a manipulable feature of multichannel nanoreactor for practical applications.

To be more precise on this point, we added the references about other iron-containing mesoporous silica-based catalysts in phenol hydroxylation to dihydroxybenzene for comparison. In Table 6, some typical results reported in the literature are summarized. Compared with the irregular Fe-containing catalysts, such as 8Fe^[20] and 2Fe-Si,^[7] although Fe-NTR 5R3 has lower iron content, it exhibited a relatively higher catalytic performance. This finding suggests that the regular tube morphology as well as the parallel multichannel structure of Fe-NTRs plays an essential role for the enhanced catalytic performance of the nanoreactors. Notably, compared with Fe-MCM-41 NPs(120) that has spherical morphology with 120 nm in diameter and similar iron content to Fe-NTR, the catalytic activity of 5R3 obtained at room temperature is higher than that of Fe-MCM-41 NPs(120) at 60 °C. This observation indicates that the longer channel should be favorable to the enhancement of conversion rate phenol hydroxylation reaction, which is in agreement with the experimental result.

Stability of Fe-NTRs

The test of the reusability of Fe-NTRs was conducted with sample 5R3 as representative. We found that the conversion of phenol decreased from 48.8% (fresh catalyst), 41.5% (first recycle) to 31.3% (second recycle). Simultaneously, the Fe contents determined by ICP-MS after each cycle of reaction were decreased from 0.65, 0.52 to 0.47 wt%. The deactivation of the Fe-NTR 5R3 in phenol hydroxylation could be partially attributed to the gradual leaching of iron species. The selectivity to dihydroxybenzene is in the range of 52.3% to 58.5%. The result indicated that the iron species incorporated in the silicate framework of Fe-NTR are more resistant to the leaching and necessary for the stability of the iron-containing silicate catalyst.^[20] The multichannel structure and the tubular morphology of the Fe-NTRs were still preserved after reuse, as shown in Figure S6.

Conclusions

We developed a novel one-step solubilization (OSS) strategy for constructing Fe-containing multichannel mesoporous silicate nanotube reactors (Fe-NTRs). cetyltrimethylammonium bromide (CTAB) was used as structure-directing agent to form mesopores of Fe-NTRs. The ferrocene was chosen as the metal precursor, which was introduced into Fe-NTRs by solubilizing inside the hydrophobic core of CTA⁺. PEO₂₀PPO₇₀PEO₂₀ (P123,

$M_n \approx 5800$) was applied as a shape-controlling additive to modulate the morphology of nanotubes. The ordered multichannel mesopore structure and regular tube morphology are well-preserved in Fe-NTRs. The sizes of Fe-NTRs are manipulable. For the Fe-NTRs with lower iron loading amount, most of iron species are incorporated into the framework of mesoporous silica. With the increasing amount of iron loading, more extra-framework iron species were produced. The iron species with tetrahedral coordination in the framework of Fe-NTR were favorable and effective for the phenol hydroxylation reaction. In contrast, the oligomeric extra-framework iron results in lower conversion rate of phenol and dihydroxybenzene selectivity. The catalytic activity of Fe-NTRs can be well-regulated by the fine control of size and morphology of nanoreactors. The OSS strategy is a simple, controllable, and efficient process, and also applicable to the preparation of Ti and Zr-containing silicate tube nanoreactors. The present strategy of integrating the functions of the tube morphology, multichannel mesopores, controllable sizes, and active sites reveals a simple and flexible access to the design and synthesis of a novel class of functional silicate nanoreactors.

Experimental Section

Chemicals

CTAB, ($C_{16}H_{33}(CH_3)_3NBr$, 99%) was purchased from J&K Chemical Ltd. PEO₂₀PPO₇₀PEO₂₀ (P123, $M_n \approx 5800$) was purchased from Sigma-Aldrich Co. TEOS (AR), ferrocene ($C_{10}H_{10}Fe$, AR) and phenol (C_6H_5OH , AR) were purchased from Sinopharm Chemical Reagent Co., Ltd. Ammonia solution (25 wt%) and hydrogen peroxide (H_2O_2 , 30 wt%) were purchased from Nanjing Chemical Reagent Co., Ltd. Titanocene dichloride ($C_{10}H_{10}Cl_2Ti$, 97%) and zirconocene dichloride ($C_{10}H_{10}Cl_2Zr$, 98%) were purchased from Aladdin Industrial Co.

Preparation

All chemicals were used as received without further purification.

Fe-NTRs with varied iron contents: In a typical run, CTAB, P123, and ferrocene were dissolved in concentrated ammonia (100 mL, NH_3 , 25 wt%) with a stirring of 300 rpm at 40 °C. The concentrations of CTAB and P123 in the mixed solution were 10.98 mm and 1.73×10^{-1} mm, respectively. After stirring for 1 h, TEOS (2 mL) was dripped into the mixed solution. Then, the mixture was continuously stirred for an additional 3 h. The resulting products were collected by filtration and dried at RT. The organic components were removed by calcination at 500 °C for 5 h. By altering the input amount of ferrocene, a series of Fe-NTRs with varied iron contents were obtained. They are designated as xR: 5R, 10R, 15R, and 20R, respectively, where x is 100 times of the calculated molar ratio of ferrocene/silicon used in the synthesis gel.

Fe-NTRs with controllable sizes: Fe-NTRs with controllable sizes were achieved by altering the input amount of P123 under the above conditions. These samples were labeled as 5Rn: 5R1 (2.59×10^{-1} mm P123), 5R2 (1.73×10^{-1} mm P123), 5R3 (1.04×10^{-1} mm P123), 5R4 (6.90×10^{-2} mm P123), and 5R5 (3.45×10^{-2} mm P123). n from 1 to 5 represents an increasing length of Fe-NTRs.

Characterization

The XRD patterns of the samples were collected with a diffractometer (RigakuD/Max-RAX) equipped with a rotating anode and $Cu_{K\alpha}$ radiation ($\lambda = 0.154178$ nm). N_2 physisorption isotherms were measured on a Micromeritics ASAP-2020 analyzer at 77 K. Before the measurements, calcined samples were degassed in vacuum at 200 °C for 3 h. Surface areas were calculated using the BET equation and pore size distributions were obtained by the Barrett-Joyner-Halenda (BJH) method using desorption branch data. FTIR spectra were recorded with Bruker VECTOR22 FTIR spectrometer in the range of 4000–400 cm^{-1} . Field-emission scanning electron microscopy was performed on a Hitachi S4800 Field Emission Scanning Electron Microscopy. HRTEM images were recorded on a JEM-2010 EX microscope operated at an accelerating voltage of 200 kV. The samples were crushed in A.R. grade ethanol and the resulting suspension was allowed to dry on carbon film supported on copper grids. The iron content in the samples was determined using a Jarrell-Ash 1100 Inductively Coupling Plasma mass spectrometry (ICP-MS). The samples were completely dissolved in hydrofluoric acid before analysis. Diffuse reflectance UV/Vis spectra were recorded by a PerkinElmer Lambda 35 spectrophotometer in the range of 200–800 nm with $BaSO_4$ as reference. The XPS were conducted on PHI 5000 Versa Probe X-ray photoelectron spectrometer equipped with $Al_{K\alpha}$ radiation (1486.6 eV). The C1s peak at 284.6 eV was used as the reference for binding energies.

Catalytic test

The direct oxidation of phenol to dihydroxybenzene was performed according to the following procedure. catalyst (0.02 g) and phenol (0.4 g) were added to deionized water 10 mL in a 50 mL flask at RT. Then, H_2O_2 (0.26 mL (30 wt%)) was dripped into the above mixture with a magnetic stirring. The molar ratio of phenol/ H_2O_2 was 3:2. After all H_2O_2 was added, the reaction mixture was stirred for an additional 5 h. After high speed centrifugation, the supernatant was obtained and analyzed by an Agilent 1100 HPLC equipped with a reversed phase C18 column. The used catalyst was filtrated, dried and calcined at 500 °C before being recycled.

Diffusion properties

Phenol loading: Samples of 0.1 g representative Fe-NTRs (5R1 and 5R4) were added to phenol (15 mL, 0.2 g) aqueous solution at room temperature. Then the test tubes were sealed to prevent water from evaporation. After the dispersion of Fe-NTRs by ultrasound, the mixture was vigorously stirred for 12 h. The phenol-loaded Fe-NTRs was obtained by centrifugation at 5000 rpm for 10 min, washed with 45 mL deionized water and then dried in air at 35 °C. Phenol-loaded Fe-NTRs powder (0.06 g) was immersed into 12 mL water. After ultrasonic treatment (1 min), the mixture was stirred at a constant rate of 300 rpm. A 2 mL volume of the suspension was extracted at given time intervals and centrifuged at 10000 rpm for UV/Vis analysis at the wavelength of 210 nm. The release profile was plotted using the average data from three independent experiments.

Acknowledgements

This work was supported by the National Natural Science Foundations of China (No. 21276125, 21476108), the Program for Scientific Innovation Research of College Graduates in Jiangsu Prov-

ince (No. CXZZ13_0443), the Key Program of National Natural Science Foundation of China (No. 21136005) and the Project of Priority Academic Program Development of Jiangsu Higher Education Institutions (PAPD).

Keywords: iron • mesoporous materials • nanotubes • surfactants • synthetic methods

- [1] B. Louis, G. Laugel, P. Pale, M. M. Pereira, *ChemCatChem* **2011**, *3*, 1263–1272.
- [2] a) Y. Yang, X. Liu, X. B. Li, J. Zhao, S. Y. Bai, J. Liu, Q. H. Yang, *Angew. Chem. Int. Ed.* **2012**, *51*, 9164–9168; *Angew. Chem.* **2012**, *124*, 9298–9302; b) Z. M. Cui, Z. Chen, C. Y. Cao, L. Jiang, W. G. Song, *Chem. Commun.* **2013**, *49*, 2332–2334; c) S. Crossley, J. Faria, M. Shen, D. E. Resasco, *Science* **2010**, *327*, 68–72; d) D. J. Cole-Hamilton, *Science* **2010**, *327*, 41–42.
- [3] a) S. J. Ding, J. S. Chen, G. G. Qi, X. N. Duan, Z. Y. Wang, E. P. Giannelis, L. A. Archer, X. W. Lou, *J. Am. Chem. Soc.* **2011**, *133*, 21–23; b) G. Zhang, J. Long, X. Wang, Z. Zhang, W. Dai, P. Liu, Z. Li, L. Wu, X. Fu, *Langmuir* **2010**, *26*, 1362–1371; c) A. Stein, B. J. Melde, R. C. Schroden, *Adv. Mater.* **2000**, *12*, 1403–1419.
- [4] H. Q. Wang, J. Chen, Y. Wu, X. Y. Xu, J. Wang, Y. Kong, *RSC Adv.* **2014**, *4*, 50832–50839.
- [5] C. X. Jiang, K. Hara, A. Fukuoka, *Angew. Chem. Int. Ed.* **2013**, *52*, 6265–6268; *Angew. Chem.* **2013**, *125*, 6385–6388.
- [6] A. I. Carrillo, E. Serrano, R. Luque, J. Garcia-Martinez, *Appl. Catal. A* **2013**, *453*, 383–390.
- [7] X. Liang, R. Yang, G. Li, C. Hu, *Microporous Mesoporous Mater.* **2013**, *182*, 62–72.
- [8] J. F. Lin, B. H. Zhao, Y. Cao, H. Xu, S. H. Ma, M. Y. Guo, D. R. Qiao, Y. Cao, *Appl. Catal. A* **2014**, *478*, 175–185.
- [9] J. Fan, W. Q. Shui, P. Y. Yang, X. Y. Wang, Y. M. Xu, H. H. Wang, X. Chen, D. Y. Zhao, *Chem. Eur. J.* **2005**, *11*, 5391–5396.
- [10] a) J. J. Xie, Y. Y. Duan, S. A. Che, *Adv. Funct. Mater.* **2012**, *22*, 3784–3792; b) V. V. Pushkarev, K. An, S. Alayoglu, S. K. Beaumont, G. A. Somorjai, *J. Catal.* **2012**, *292*, 64–72; c) A. Zürner, J. Kirstein, M. Dobliger, C. Brauchle, T. Bein, *Nature* **2007**, *450*, 705–708; d) A. Nisar, Y. Lu, J. Zhuang, X. Wang, *Angew. Chem. Int. Ed.* **2011**, *50*, 3187–3192; *Angew. Chem.* **2011**, *123*, 3245–3250.
- [11] a) T. Suteewong, H. Sai, R. Hovden, D. Muller, M. S. Bradbury, S. M. Gruner, U. Wiesner, *Science* **2013**, *340*, 337–341; b) M. Egi, K. Sugiyama, M. Saneto, R. Hanada, K. Kato, S. Akai, *Angew. Chem. Int. Ed.* **2013**, *52*, 3654–3658; *Angew. Chem.* **2013**, *125*, 3742–3746; c) V. S. Y. Lin, D. R. Radu, M. K. Han, W. H. Deng, S. Kuroki, B. H. Shanks, M. Pruski, *J. Am. Chem. Soc.* **2002**, *124*, 9040–9041.
- [12] S. H. Wu, C. Y. Mou, H. P. Lin, *Chem. Soc. Rev.* **2013**, *42*, 3862–3875.
- [13] a) F. Tang, L. Li, D. Chen, *Adv. Mater.* **2012**, *24*, 1504–1534; b) S. Che, Z. Liu, T. Ohsuna, K. Sakamoto, O. Terasaki, T. Tatsumi, *Nature* **2004**, *429*, 281–284.
- [14] T. W. Kim, M. J. Kim, F. Kleitz, M. M. Nair, R. Guillet-Nicolas, K. E. Jeong, H. J. Chae, C. U. Kim, S. Y. Jeong, *ChemCatChem* **2012**, *4*, 687–697.
- [15] a) A. N. Khlobystov, *ACS Nano* **2011**, *5*, 9306–9312; b) K. S. Ha, G. Kwak, K. W. Jun, J. Hwang, J. Lee, *Chem. Commun.* **2013**, *49*, 5141–5143; c) Z. Y. Zhao, J. F. Tian, Z. X. Wu, J. Liu, D. Y. Zhao, W. Shen, L. Z. He, *J. Mater. Chem. B* **2013**, *1*, 4719–4722; d) K. Kageyama, J. Tamazawa, T. Aida, *Science* **1999**, *285*, 2113–2115.
- [16] J. Kim, C. Anand, S. N. Talapaneni, J. You, S. S. Aldeyab, E. Kim, A. Vinu, *Angew. Chem. Int. Ed.* **2012**, *51*, 2859–2863; *Angew. Chem.* **2012**, *124*, 2913–2917.
- [17] a) X. L. Huang, L. L. Li, T. L. Liu, N. J. Hao, H. Y. Liu, D. Chen, F. Q. Tang, *ACS Nano* **2011**, *5*, 5390–5399; b) T. Yu, A. Malugin, H. Ghandehari, *ACS Nano* **2011**, *5*, 5717–5728.
- [18] a) Y. M. Liu, J. Xu, L. He, Y. Cao, H. Y. He, D. Y. Zhao, J. H. Zhuang, K. N. Fan, *J. Phys. Chem. C* **2008**, *112*, 16575–16583; b) Z. Sun, B. Sun, M. Qiao, J. Wei, Q. Yue, C. Wang, Y. Deng, S. Kalliaguine, D. Zhao, *J. Am. Chem. Soc.* **2012**, *134*, 17653–17660; c) C. Liu, J. Li, J. Qi, J. Wang, R. Luo, J. Shen, X. Sun, W. Han, L. Wang, *ACS Appl. Mater. Interfaces* **2014**, *6*, 13167–13173; d) K. Kandel, J. W. Anderegg, N. C. Nelson, U. Chaudhary, I. I. Slowing, *J. Catal.* **2014**, *314*, 142–148; e) M. Popova, A. Ristic, K. Lazar, D. Maucec, M. Vassileva, N. N. Tusar, *ChemCatChem* **2013**, *5*, 986–993; f) H. Xin, J. Zhao, X. Li, J. Tang, Q. Yang, *Microporous Mesoporous Mater.* **2014**, *190*, 54–62; g) Y. Zhao, Y. Zhang, J. Chen, J. Li, K. Liew, M. R. Bin Nordin, *ChemCatChem* **2012**, *4*, 265–272.
- [19] H. Q. Wang, S. Y. Gao, J. Du, J. Chen, Y. Kong, J. Wang, *Appl. Catal. A* **2015**, *504*, 228–237.
- [20] C. Wu, Y. Kong, F. Gao, Y. Wu, Y. N. Lu, J. Wang, L. Dong, *Microporous Mesoporous Mater.* **2008**, *113*, 163–170.
- [21] Y. Yang, C. J. Sun, Y. Ren, S. J. Hao, D. Q. Jiang, *Sci. Rep.* **2014**, *4*, 4540.
- [22] C. Bosch-Navarro, E. Coronado, C. Marti-Gastaldo, P. Amoros, *Nanoscale* **2014**, *6*, 7981–7990.
- [23] K. Mori, T. Yamaguchi, S. Ikurumi, H. Yamashita, *Chem. Commun.* **2013**, *49*, 10468–10470.
- [24] T. Zhang, P. Gao, C. Gao, H. Yang, Y. Zhao, *Chinese J. Catal.* **2010**, *31*, 701–704.
- [25] A. Papat, J. Liu, Q. Hu, M. Kennedy, B. Peters, G. Q. Lu, S. Z. Qiao, *Nanoscale* **2012**, *4*, 970–975.
- [26] T. W. Kim, P. W. Chung, V. S. Y. Lin, *Chem. Mater.* **2010**, *22*, 5093–5104.
- [27] a) K. Schillén, J. Jansson, D. Lof, T. Costa, *J. Phys. Chem. B* **2008**, *112*, 5551–5562; b) Y. Han, H. Yu, H. Du, W. Jiang, *J. Am. Chem. Soc.* **2010**, *132*, 1144–1150.
- [28] K. Suzuki, K. Ikari, H. Imai, *J. Am. Chem. Soc.* **2004**, *126*, 462–463.
- [29] R. Peng, C. M. Wu, J. Baltrusaitis, N. M. Dimitrijevic, T. Rajh, R. T. Koodali, *Chem. Commun.* **2013**, *49*, 3221–3223.
- [30] A. Ramanathan, B. Subramaniam, R. Maheswari, U. Hanefeld, *Microporous Mesoporous Mater.* **2013**, *167*, 207–212.
- [31] a) L. Shi, X. Q. Zhu, Y. Su, W. Z. Weng, H. Feng, X. D. Yi, Z. X. Liu, H. L. Wan, *J. Catal.* **2013**, *307*, 316–326; b) C. H. Cui, H. H. Li, J. W. Yu, M. R. Gao, S. H. Yu, *Angew. Chem. Int. Ed.* **2010**, *49*, 9149–9152; *Angew. Chem.* **2010**, *122*, 9335–9338.
- [32] Y. Jiang, K. Lin, Y. Zhang, J. Liu, G. Li, J. Sun, X. Xu, *Appl. Catal. A* **2012**, *445*, 172–179.
- [33] N. S. Sanjini, S. Velmathi, *RSC Adv.* **2014**, *4*, 15381–15388.
- [34] H. J. Kim, J. E. Ahn, S. Haam, Y. G. Shul, S. Y. Song, T. Tatsumi, *J. Mater. Chem.* **2006**, *16*, 1617–1621.
- [35] J. V. Coelho, M. S. Guedes, R. G. Prado, J. Tronto, J. D. Ardisson, M. C. Pereira, L. C. A. Oliyeyra, *Appl. Catal. B* **2014**, *144*, 792–799.
- [36] F. Hayashi, K. I. Ishizu, M. Iwamoto, *Eur. J. Inorg. Chem.* **2010**, 2235–2243.
- [37] R. Kumar, P. Mukherjee, A. Bhaumik, *Catal. Today* **1999**, *49*, 185–191.
- [38] E. Gross, J. H. C. Liu, F. D. Toste, G. A. Somorjai, *Nat. Chem.* **2012**, *4*, 947–952.

Received: August 3, 2015

Published online on November 3, 2015